Evaluating high frequency fluctuations and its effect on hemodynamics at varying heart rates in intracranial aneurysms via 4D PTV

Baha Al-Deen T. El-Khader[1], Jibin Joy Kolliyil[1], Jana Korte[2,3], Nikhil S. Shirdade[1], Ephraim W. Church[4], Melissa C. Brindise[1,*]

1: Dept. of Mechanical Engineering, Pennsylvania State University, USA
2: STIMULATE Research Campus, University of Magdeburg, Magdeburg, Germany
3: Laboratory of fluid dynamics and technical flows, University of Magdeburg, Magdeburg, Germany
4: Department of Neurosurgery, Penn State Health, USA
*Corresponding author: mcb5351@psu.edu

Keywords: Particle tracking velocimetry (PTV), cerebral aneurysms, heart rate, high-frequency fluctuations.

ABSTRACT

Hemodynamics have been shown to affect the growth and rupture of intracranial aneurysms (IA). Studies have increasingly reported the presence of high frequency velocity fluctuations in aneurysms. However, it remains undetermined how transient physiological factors like heart rate and inflow blood waveform amplitude affect the hemodynamic parameters and high frequency fluctuations in and around an IA, as well as the risk of IA progression. In this work, we address this question using a volumetric particle tracking velocimetry (PTV) study where a patient-specific right middle cerebral artery (R MCA) aneurysm model was subjected to two heart rate conditions (60 bpm and 137 bpm). The input waveform amplitude for the 137 bpm case was increased by a factor of 1.6 to be physiologically consistent. Captured PTV images were processed using the Shake-the-Box (STB) workflow. Flow parameters including velocity, vorticity, and turbulent kinetic energy (TKE) were evaluated. To evaluate the presence of high frequency fluctuations, a direct numerical simulation (DNS) using the R MCA geometry and same two heart rate cases was conducted and a method for use with STB particle tracks was proposed. As compared to the 60 bpm case, the 137 bpm case had a more concentrated inflow jet that extended further into the aneurysmal sac and a stronger and larger vortical flow structure in the aneurysmal sac. The 60 bpm case maintained a region of slightly elevated TKE at the main junction point where the aneurysmal sac and all vessels merge. In the 137 bpm case, TKE in this region was dramatically higher. Using probe points, the DNS data revealed high frequency velocity fluctuations in an outflow vessel during the deceleration phase of the cycle. Notably, these fluctuations were only observed for the 137 bpm case. For both the DNS and STB data, high frequency components were more prevalent and stronger outside of the aneurysmal sac as opposed to inside the aneurysmal sac. Overall, these results suggest that changes in heart rate induce changes to the flow structure and can induce significant increases in TKE and high frequency fluctuations. Based on our findings, a higher heart rate would be expected to yield a flow field more akin to IA progression. The specific correlation between the high frequency components computed using our proposed STB-based method and the high frequency fluctuations in the flow field could not be well understood. Thus, additional analysis and development of this method is needed.

1. Introduction

An aneurysm is a pathological condition characterized by the dilation and thinning of a portion of the arterial walls. Studies have estimated that 3% of the global population (Vlak et al., 2011) and between 1% to 6% of the adult population in the United States (Rinkel et al., 1998; Schievink, 1997) harbors an unruptured intracranial aneurysm (IA). The rupture of an IA is associated with high (>50%) mortality and morbidity rates (Mayberg et al., 1994; Brisman et al., 2006). However, clinicians struggle to assess the risk versus reward balance for intervention of unruptured IAs. Specifically, clinicians must determine if the likelihood of aneurysm rupture outweighs the intervention procedure risk which carries a 5-7% morbidity rate. It is estimated that over two-thirds of all aneurysms are stable and will not rupture through the patient's lifetime. However, uncertainty surrounding the mechanisms driving the formation, growth, and rupture of an IA make assessing an individual IA's risk of progression a significant challenge.

Previous studies have concluded that hemodynamics play an important role in the growth and rupture of an IA (Cebral & Raschi, 2013; Yagi et al., 2013; Roloff et al., 2019; Xiang et al., 2011; Meng et al., 2014). For example, Boussel et al. (2008) reported that aneurysms grow at regions of low wall shear stress (WSS). However, regions of both high and low WSS have been associated with aneurysm growth (Meng et al., 2014). High flow complexity and unstable flow patterns that change throughout the pulsatile cycle have been linked to increased risk of IA progression (Cebral et al., 2011a; Xiang et al., 2011; Cebral & Raschi, 2013; Qian et al., 2011). Other studies have reported the presence of high turbulent kinetic energy (TKE) in and around aneurysms (Yagi et al., 2013). In fact, Saqr et al. (2020) concluded that IA flow—despite its low Reynolds number on the order of 300—is turbulent. The presence of TKE and turbulent-like flow is believed to increase risk of IA rupture. However, IAs with stable flow patterns have been shown to rupture (Valen-Sendstad et al., 2013). Hence, while hemodynamics is broadly accepted to affect an IA's risk of progression, its specific role remains unclear.

The potential presence of high frequency fluctuating flow components within an IA has received increased attention in recent years. Prior studies have observed high frequency fluctuations in IAs through *in vivo*, *in vitro*, and *in silico* modalities. For *in vivo* studies, the high frequency fluctuations were observed through audible thrills or murmurs (H. Steiger & Reulen, 1986; Ferguson, 1970; Sekhar & Wasserman, 1984). *In vitro* studies have employed experimental glass models to investigate these instabilities (Roach et al., 1972; H. J. Steiger et al., 1987, 1988). Roach et al. (1972) and H. J. Steiger et al. (1987) reported instabilities and disturbed flow in aneurysms at sharp bifurcations (e.g, 90°) even at low Reynolds numbers (400). Also, high-resolution computational fluid dynamics (CFD) studies have detected high frequency fluctuations in aneurysmal flow (Valen-Sendstad et al., 2013, 2014; Ford & Piomelli, 2012). Such instabilities can affect key hemodynamic parameters that drive the growth of an IA. For example, previous CFD studies have reported these flow instabilities affect the magnitude and direction of WSS (Baek et al., 2010; Valen-Sendstad et

al., 2011). However, the specific association between high frequency fluctuations and aneurysm growth and rupture is still unclear. For instance, a study has linked the growth regions of IAs to flow instabilities (Dabagh et al., 2019), while another reported a correlation between clinical history of a ruptured aneurysm and unstable flow patterns (Cebral et al., 2011a). On the other hand, two previous studies quantified flow instability using the spectral power index (SPI) (Khan et al., 2021) and fluctuation kinetic energy (fKE) (Varble et al., 2016). In both studies, no association between flow instability and aneurysm rupture was found.

Additionally, the rupture of the IA is usually associated with extreme physical exertion and/or emotional excitement, events that are typically also accompanied by abrupt substantial changes in both heart rate and blood pressure. However, only a small number of studies have investigated the effect of elevated heart rate values on the hemodynamics of IA's (Bowker et al., 2010; Jiang & Strother, 2009; Sarrami-Foroushani et al., 2016). These studies have been predominantly CFD studies which still struggle with clinical acceptance due to limited CFD validation and disputed CFD assumptions such as laminar flow (Berg et al., 2014). Additionally, conflicting finding have been reported regarding the relationship between heart rate and hemodynamic parameters. For instance, Jiang & Strother (2009) have reported a large increase in WSS with the increase in heart rate. On the other hand, Bowker et al. (2010) reported no significant changes in WSS at higher heart rate conditions. Finally, Sarrami-Foroushani et al. (2016) reported an overall small increase in WSS at higher heart rates. However, they observed inconsistent results at regions of exceptionally low or high WSS.

In this study, we aim to: 1) investigate the effects of heart rate and inflow amplitude on IA hemodynamics using 4D particle tracking velocimetry (PTV); 2) explore the extent to which high frequency fluctuations are observed in the flow using both our experimental dataset and corresponding direct numerical simulation (DNS) data; and 3) evaluate how observed high frequency fluctuations change with heart rate.

2. Methods

2.1. IA Geometry and Flow Loop

A schematic of the flow loop and volumetric PTV setup used for this study is given in Fig. (1). The working fluid was a blood analog consisting of water, glycerol, and urea (Brindise et al., 2018). This solution has been shown to enable good agreement with both the density and viscosity of blood. The density of the used working fluid was 1141.76 kg/m^3 and kinematic viscosity was 3.468×10^{-6} m^2/s. We manufactured an *in vitro* polydimethylsiloxane (PDMS) Sylgard 184 model of a patient-specific right middle cerebral artery (R MCA) aneurysm which maintained the same refractive index as the working fluid (n = 1.4130). The used R MCA model is shown in Fig. (2). The R MCA

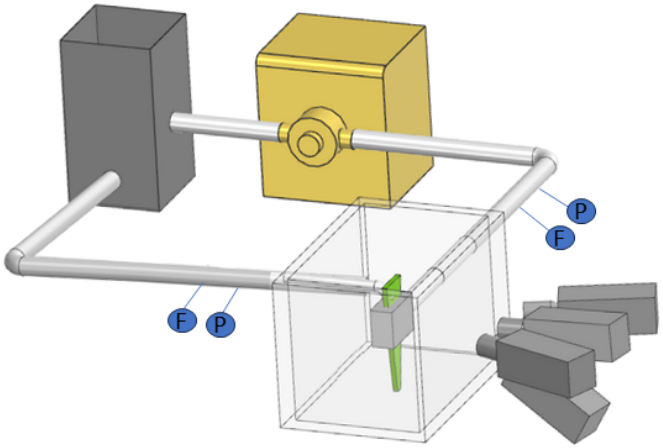

Figure 1. Schematic of flow loop.

model was inserted into the physiological flow loop. Two heart rate conditions were considered for this study including a 60 bpm and a 137 bpm case. Because heart rate increases are intrinsically associated with blood flow velocity increases, the peak inflow amplitude was increased by a factor of 1.6 for the 137 bpm case. The inflow waveforms for the 60 bpm case and the 137 bpm case are shown in Fig. (3). A computer-controlled gear pump was used to generate the pulsatile inflow waveforms. Moreover, at least 150-diameter length of tubing was included before the aneurysm inlet to ensure a fully developed flow profile. An ultrasonic flowmeter (Transonic) was placed upstream of the aneurysm inlet and pressure transducers (Omega, PX309) were placed before the inlet and after both outlets of the aneurysm to monitor the flow loop properties.

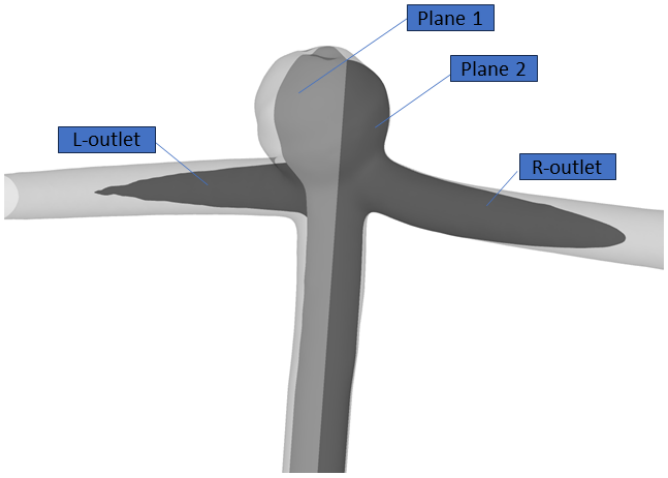

Figure 2. R MCA aneurysm model.

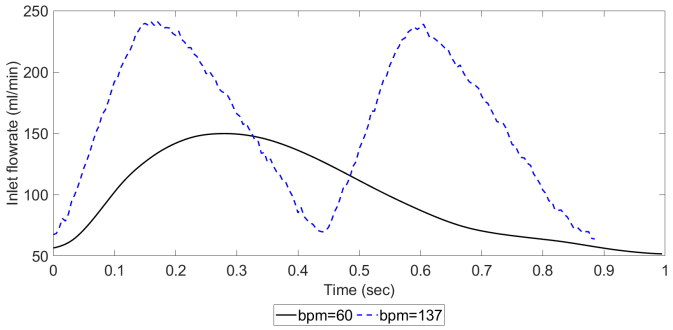

Figure 3. Inflow waveform for 60 bpm and 137 bpm cases.

2.2. PTV Measurement Technique

PTV images were captured using four high speed-cameras (Phantom VEO440) and an Nd-YLF laser (Photonic Industries, λ=527 nm). To ensure a maximum particle displacement of 18 pixels between frames, images were captured a frequency of 1600 Hz and 2500 Hz for the 60 bpm and 137 bpm cases, respectively. Images were captured at a resolution of 1280 x 852 pixels. This resulted in each camera's magnification being around 18.36 µm/pixel. The working fluid was seeded with 19 μm fluorescent particles. Cameras in the setup, except the center camera, were angled approximately 30^o from the front plane of the aneurysm and optical long pass filters were mounted on each camera to filter out the laser light wavelength from the images. Additionally, the aneurysm geometry was submerged in a refractive index matched (n=1.4130) fluid consisting of water and glycerol to reduce optical distortion. The camera's hardware limitations and the desired particle displacement allowed for the capture of 13 cycles for the 60 bpm case and 20 cycles for the 137 bpm case.

Davis 10.0 (LaVision Inc.) software was used to process the particle images. A two-level calibration target and the polynomial fit method for the camera calibration was used. In this method, coplanar equidistant views are recorded for camera calibration to account for the z dependence (depth) needed to achieve a volume mapping of the field of view to the camera's chip. The average perspective error for the cameras was approximately 0.49. This error was corrected to 0.0075 through the iterative volumetric self-calibration process (Wieneke, 2008). Shake-the-box (STB) (Schanz et al., 2016) was used here to perform time-resolved three-dimensional particle tracking. This method produces a Lagrangian velocity field displayed as particles tracks. With STB, the location of a particle in the next time step is predicted using the velocity of the particle in the current time step and then optimized by 'shaking' of the spatial position of the predicted particle to minimize the disparity between the predicted particle and the actual particle in the camera images. For IA studies, STB has been shown to significantly reduce ghost particles and computation time, as compared to using tomographic particle image velocimetry (TOMO-PIV) (Brindise et al., 2019). For the STB processing, the allowed triangulation error was set to 3.0 voxels. The outer loop (adding particles)

was set to 12 iterations and the inner loop (refining particle position) was set to 8 iterations. Also, particle position shaking was set to 0.8 voxels and particles closer than 0.1 voxels were removed.

STB velocity fields were registered and masked by the STL geometry obtained from a micro-computed tomography (CT) scan of the aneurysm model. To calculate and analyze hemodynamic parameters, STB velocity fields were converted from a Lagrangian to an Eulerian setting. Thus, STB velocity fields were gridded to an isotropic resolution of 0.3 mm^3. To increase the accuracy of the STB gridding, a temporal grouping of the STB velocity fields (4:1) was done which increased the number of particles used for the averaging calculation in each voxel. However, this reduced the temporal resolution to 2.5 × 10^{-3} sec and 1.6 × 10^{-3} sec for the 60 bpm and 137 bpm cases, respectively. The gridded STB velocity fields were then denoised using proper orthogonal decomposition (POD) (Sirovich, 1989) with the entropy line fit thresholding (ELF) criterion (Brindise & Vlachos, 2017) and one pass of universal outlier detection (UOD) with a window size of 5x5x5 and a tolerance threshold of 2.5 (Westerweel & Scarano, 2005). Subsequently, phase averaging of the resultant pulsatile velocity fields was done. For both heart rate cases, 13 cycles were used for the phase averaging (even though 20 cycles were captured with the 137 bpm case) to minimize the likelihood of inconsistent smoothing of the velocity fields from this operation. The gridded, denoised, and phase averaged STB velocity fields were used for all post-processing and will be referred to as 'velocity fields' in the Results section.

2.3. Post-processing

Vorticity and turbulent kinetic energy (TKE) were computed for each heart rate case. Vorticity was computed as shown in equations below:

$$\omega_x = (\frac{\delta w}{\delta y}) - (\frac{\delta v}{\delta z}) \tag{1}$$

$$\omega_y = (\frac{\delta u}{\delta z}) - (\frac{\delta w}{\delta x}) \tag{2}$$

$$\omega_z = (\frac{\delta v}{\delta x}) - (\frac{\delta u}{\delta y}) \tag{3}$$

where ω_x is the 2D vorticity in yz-plane, ω_y is the 2D vorticity in xz-plane, ω_z is the 2D vorticity in xy-plane, and u, v, and w are the velocity in the x,y, and z directions, respectively. To compute TKE, the Reynolds decomposition was needed to calculate the fluctuating velocity. The Reynolds dcomposition can be expressed as:

$$u_i'(t) = U_i(t) - \langle U(t) \rangle \tag{4}$$

where $u_i'(t)$ is the fluctuating velocity, $U_i(t)$ is the measured velocity, $\langle U(t) \rangle$ is the mean velocity, and t is time. The mean velocity was computed using the discrete wavelet transform (DWT) as detailed in Brindise & Vlachos (2018). Subsequently, TKE was calculated using according to:

$$k(t) = \frac{1}{2}(u_i'(t)^2 + v'(t)^2 + w'(t)^2 \tag{5}$$

Where $k(t)$ is the TKE, and $u_i'(t)$, $v_i'(t)$, and $w_i'(t)$ are the fluctuating velocities in x, y, and z directions, respectively.

2.4. Direct Numerical Simulation (DNS) Technique

DNS is well-suited for resolving any high-frequency velocity fluctuations that occur in a flow field. Thus, DNS simulations were used to explore locations where high-frequency fluctuations existed in the flow. An in-house DNS solver was used Abdelsamie et al. (2016). Blood density and kinematic viscosity were set to ρ = 1143 kg/m^3 and ν = 3.753 × 10^{-6} m^2/s, respectively. The time step size varied from 1E-10 s to 5E-5 s. and the mesh base size was 0.07 mm. Additionally, rigid walls and Newtonian fluid were assumed. Finally, inlet conditions were set based on the measured flow curves from the performed volumetric PTV.

3. Results and discussion

3.1. Effect of heart rate on the IA velocity field

We first investigate the velocity fields at two planes within the aneurysm to highlight differences in flow trends across heart rates. Figs. (4) and (5) show velocity fields at peak systole for Planes 1 and 2 (refer to Fig. (2) for definitions of the two planes). The velocity fields were normalized by the spatial average of velocity for each case in order to account for the altered inflow waveform amplitude between the two cases. At both Planes, the v-velocity contours show that the 137 bpm case maintained a stronger and more concentrated jet in the parent (inflow) vessel and as a result caused the inflow jet to extend further into the aneurysmal sac. Conversely, the inflow jet of the 60 bpm case is wider and weakens when reaching the aneurysmal sac. Some differences in the velocity field in the aneurysmal sac across heart rate cases can also be observed in Plane 1 (Fig. (4)), particularly in the u- and w-velocities. However, in Plane 2, the velocities are largely similar across cases. In Fig. (5), the u-velocity contours highlight an inhomogeneous flow in the right outlet vessel for the 60 bpm case that is not observed in the 137 bpm case. The flow at the junction region (where all vessels and the aneurysm sac merge) also maintains notable difference in velocity contours between cases. This, along with the aforementioned differences in the right outlet flow likely indicate that the distribution of flow entering the aneurysmal sac vs. moving immediately through the outlets was likely altered by heart rate.

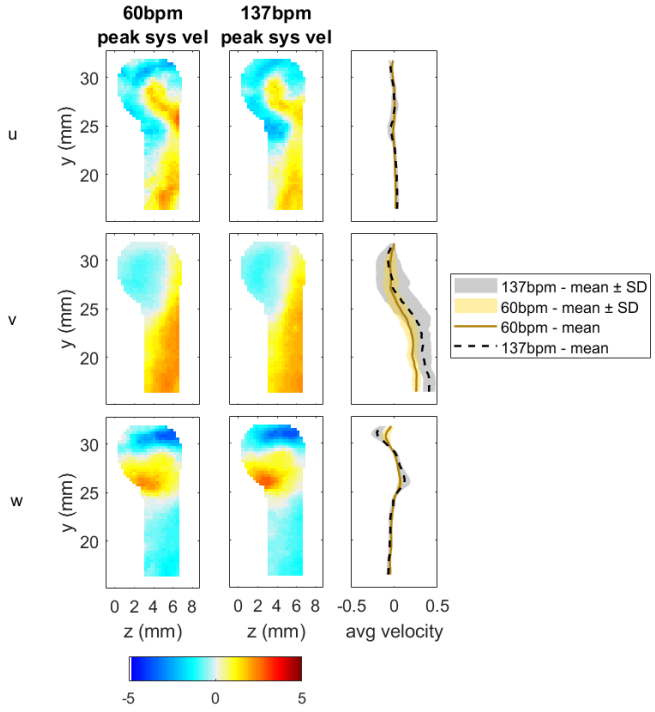

Figure 4. Normalized velocity fields at peak systole in plane 1 for 60 bpm and 137 bpm.

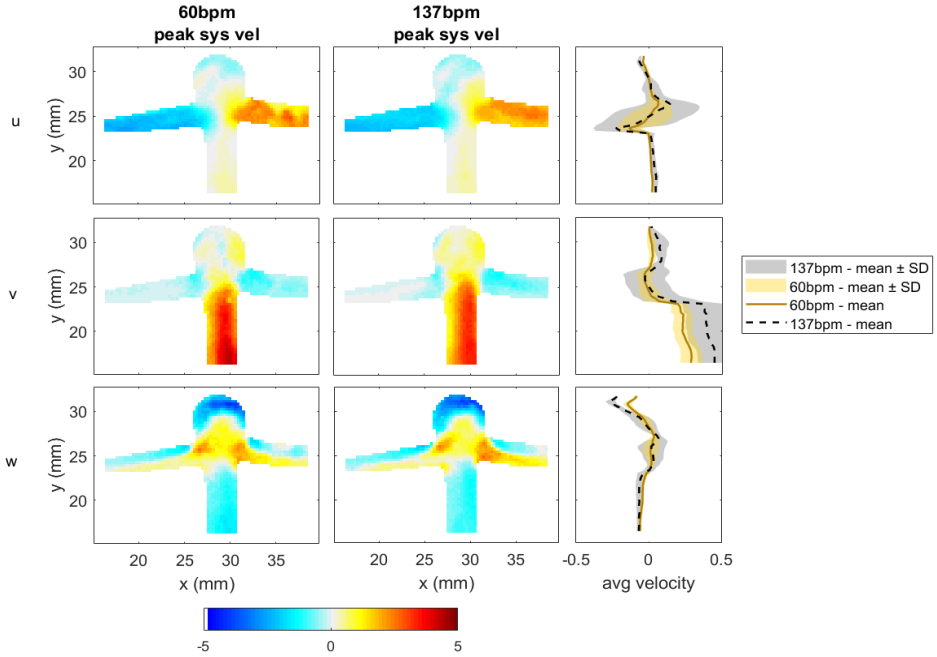

Figure 5. Normalized velocity fields at peak systole in plane 2 for 60 bpm and 137 bpm.

The variation in velocity across heart rates can be quantified using the average of the absolute point-by-point difference of the normalized velocities between the two cases cases divided by the maximum normalized velocity. For Fig. (4) the variation between 60 bpm and 137 bpm cases was 13.9%, 8.1%, 7.6% for u-vel, v-vel, w-vel, respectively. While the variation between the 60 bpm and 137 bpm cases for Fig. (5) was 7.0%, 6.5%, 7.1% for the u-, v-, and w-velocities, respectively. For all velocity components, the 137 bpm case had a higher raw velocity magnitude. Therefore, there was an agreement between velocity fields across cases.

The observed differences in the velocity fields across heart rate cases would be expected to precipitate differences in hemodynamic parameters, such as WSS, and by extension risk of IA progression. Specifically, for the 137 bpm case, we expect larger WSS values inside the aneurysmal sac, particularly at the posterior (back) side where the inflow jet persists (as shown in Fig. (4)). Additionally, a more concentrated inflow jet has been associated with increased risk of IA growth (Cebral et al., 2011a,b; Xiang et al., 2011). This would suggest that the flow field associated with the 137 bpm case may cause—to an extent—an increase in IA risk with elevated heart rate. The non-uniformity of the u-velocity in the right outflow vessel with the 60 bpm would be expected to translate to a non-uniform WSS distribution in that region, which can lead to vessel remodeling. These differences in the u-velocity could be due to the presence of a weaker inflow jet for this case which allows for secondary flows to be more apparent. Together, these finding suggest a possible trade-off exists where the lower heart rate case promotes remodeling of the vasculature surrounding the IA, while a higher heart rate promotes remodeling of the aneurysmal sac itself. This could, in part, explain why IA growth often includes simultaneous expansion of the aneurysmal sac as well as the surrounding vasculature (for example, refer to Fig. (1) in Kojima et al. (2012)).

3.2. Effect of heart rate on vorticity in and around the IA

We next explore differences in vortical flow structures across heart rates. Fig. (6) and (7) show the vorticity at peak flow rate for the two Planes. As done with velocity, the vorticity was normalized by the spatial average of vorticity for each case. In Fig. (6), vorticity-x and vorticity-y contours show the presence of a vortex in the aneurysmal sac for both bpm cases. In the 137bpm case, this vortex is stronger, more pronounced, and encompasses a larger region in the aneurysmal sac. Meanwhile, for the 60 bpm case, the vortex is weaker and more confined. Such vorticity patterns suggest the presence of recirculation zones inside the aneurysmal sac which have been associated with the presence of high frequency fluctuations and the development of regions of aneurysm growth (Ford & Piomelli, 2012; Dabagh et al., 2019).

In Plane 2, Fig. (7), the vorticity-z contour in the inflow vessel of the 137 bpm case maintains a more significant asymmetry as compared to the 60 bpm case. This asymmetry likely reflects instabilities in the inflow jet in this case. A notable difference in the vorticity-z contour at the junction between the inflow and right outflow vessels is also observed. Specifically, the 137 bpm maintains

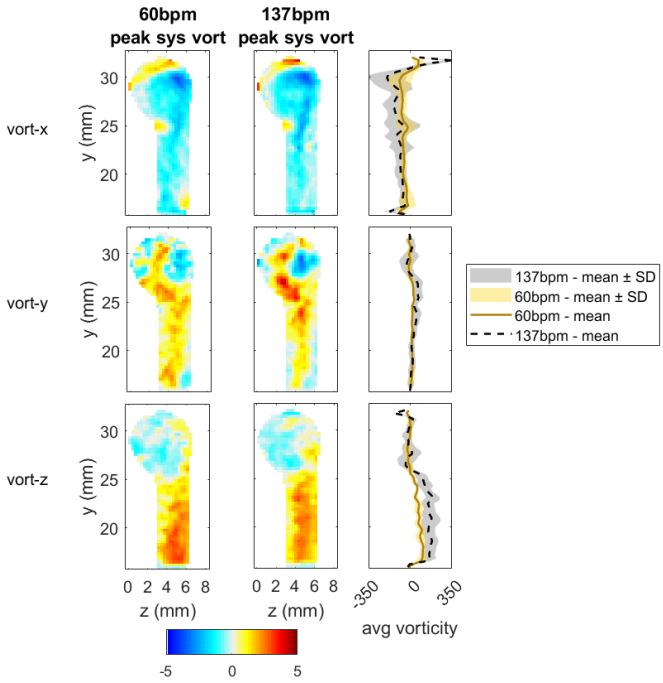

Figure 6. Flow rate at peak systole in Plane 1 for 60 bpm and 137 bpm.

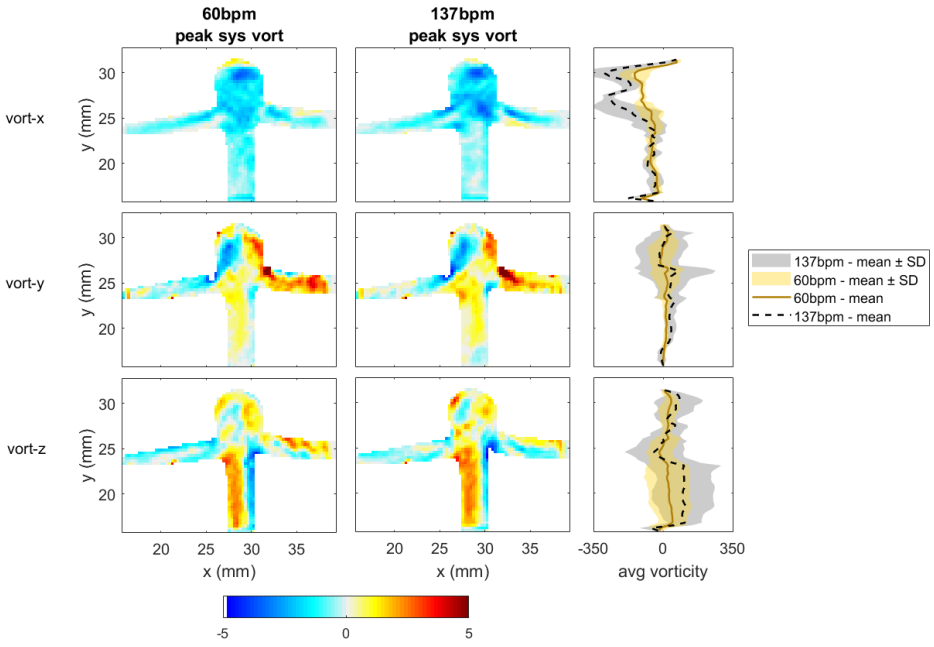

Figure 7. Flow rate at peak systole in Plane 2 for 60 bpm and 137 bpm.

a significantly higher magnitude. For both heart rate cases, high vorticity-y magnitude is observed at the junction between the aneurysmal sac and the right outflow. This high vorticity at the junctions is particularly of concern as this would likely cause high and irregular WSS magnitudes in this region. Moreover, the high curvature in these areas have been noted to yield weaker effective wall strength (Cebral et al., 2016). The 137 bpm case maintains larger vorticity-x magnitude at the junction of the vessels and aneurysmal sac as compared to the 60 bpm case. The vorticity-x in this region for the 137 bpm case is also notably unstructured. This likely indicates the presence of disturbed flow in this region, and increases the likelihood of high frequency fluctuations at this location. The variation in vorticity across heart rates was quantified using a similar method to the one used for velocity fields. Specifically, the average of the absolute point-by-point difference of the normalized vorticities between the two cases was calculated then divided by the maximum normalized vorticity. For Fig. (6) the variation between the 60 bpm and 137 bpm cases was 12.0%, 7.8%, 10.9% for vorticity-x, vorticity-y, vorticity-z, respectively. While the variation between 60 bpm and 137 bpm cases for Fig. (7) was 12.0%, 20.6%, 13.6% for vorticity-x, vorticity-y, vorticity-z, respectively. For all vorticity components, the 137 bpm case had a higher raw vorticity magnitude. Overall, such higher vorticity magnitude suggests the presence of non-uniform WSS distributions and disturbed flow at higher heart rates. This again suggests that higher heart rate might be associated with higher risk of aneurysm rupture.

3.3. Effect of heart rate on TKE in and around the IA

To more explicitly evaluate the effect of heart rate and inflow amplitude on flow instabilities in the aneurysm, Fig. (8) provides the time-averaged TKE for the two cross-sectional planes . For the 60 bpm case, high TKE is observed in the junction region where all vessels and the aneurysmal sac merge as well as in the near wall region of the right outlet. This aligns with the high vorticity magnitude observed in the near-wall regions in the right outlet (Fig. (7)). It's worth noting that there were no regions of high TKE inside the aneurysm sac for the 60 bpm case. However, relatively-speaking, larger TKE values were observed in the posterior portion of the aneurysmal sac which corresponds with regions where a strong vortex was formed, as highlighted in Figs. (6) and (7). This suggests that high vorticity values and strong vortices are associated with large TKE values and subsequently the presence of disturbed flow in IAs. A starkly different TKE distribution is observed for the 137 bpm case. Specifically, significantly larger values of TKE starting at the all-vessels junction and extending into both the aneurysmal sac and right outlet are observed. Additionally, the TKE distribution for Plane 1 pinpoints the region of high TKE to the posterior side of the aneurysmal sac (though a small region of high TKE in the anterior aneurysmal sac occurred). The TKE distribution provides the most striking indication that an elevated heart rate caused a dramatic increase in the disturbed-nature of the flow at the main junction point. This disturbed flow would be expected to lead increased variability in the flow patterns throughout a single heart

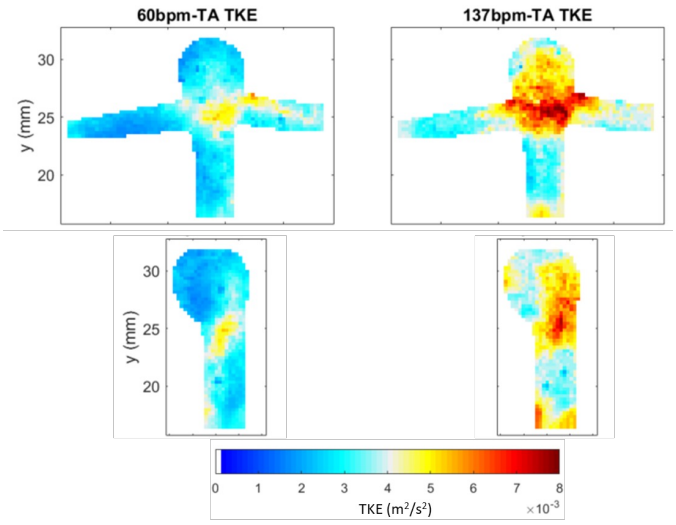

Figure 8. Time averaged TKE in Planes 1 and 2 for 60 bpm and 137 bpm.

beat as well as across heart beats. Such high TKE values and the presence of disturbed flow also strongly suggest that high frequency fluctuations are present in the aneurysmal sac and particularly in the near wall regions where higher shear gradients exist. Therefore, these results indicate that higher heart rates may be associated with the increased presence of high frequency fluctuation components in the flow. Moreover, previous studies have linked high TKE with the mechanobiology of aneurysm rupture (Valen-Sendstad et al., 2013). Thus, the risk of IA progression would be expected to be substantially higher with the higher heart rate case.

Overall, the velocity, vorticity, and TKE contours highlighted that varying heart rates seem to alter the likelihood of IA progression as well as the specific locations in the vascular that are most susceptible to remodeling. We speculate that a contributing factor to these observed differences is that at higher heart rates, acceleration gradients are inherently larger resulting in momentum forces becoming comparably more dominant than viscous forces. This is compounded by the fact that an the increase in heart rate is virtually always physiologically associated with an increase if flow amplitude. Therefore, it's challenging isolated which differences are specifically due to changes in heart rate frequency vs. changes in pulsatility amplitude. Nevertheless, previous studies have shown that flows at higher Womersely numbers (higher heart rates) had more flow instabilities and harboured more disturbed flow(Trip et al., 2012; Xu & Avila, 2018). Also, changes in heart rate are intrinsically associated with changes in the temporal gradients of velocity which have been shown to affect the rate of turbulence dissipation (Brindise & Vlachos, 2018). Therefore, despite the challenge of quantifying the isolated effect of heart rate of aneurysm thermodynamics, this work and previous work show this it's associated with increased flow instabilities and disturbed flow dynamics. This should be explored further in future work.

3.4. Evaluation of high-frequency flow fluctuations in and around the IA

The analysis of the TKE, in particular, suggests high-frequency flow fluctuations are likely to exist in the flow field. Next, we explicitly explore this notion. To date, no study (the best of our knowledge) has reported the efficacy of observing high-frequency fluctuations using STB. Thus, the DNS data provides a convenient way to identify locations where high-frequency fluctuations were definitively observed.

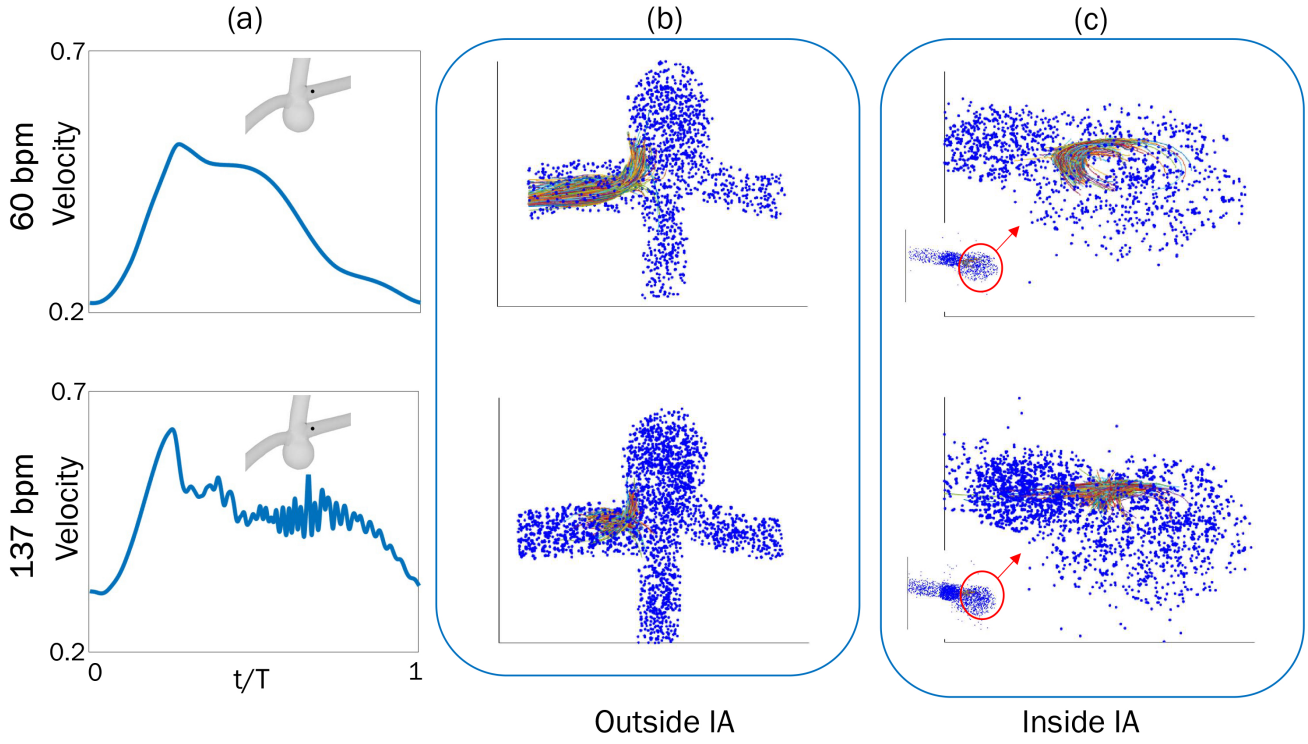

Figure 9. (a) The temporal variation of velocity magnitude at a probe point outside the aneurysmal sac using DNS data. (b) The tracks of all particles passing through the DNS probe point outside the aneurysmal sac obtained using volumetric PTV. (c) The tracks of all particle passing through a probe point inside the aneurysmal sac obtained using volumetric PTV

Fig. (9a) shows the velocity resolved from the DNS at a probe point outside of the aneurysm (as shown). For the 137 bpm case, the DNS data clearly exhibits high frequency fluctuations in the velocity during the deceleration phase. However, in the 60 bpm case, no fluctuations are observed. Considering Fig. (8), this probe point aligns with a location of high TKE in the 137 bpm, while the 60 bpm case maintained a lower magnitude and more uniform TKE distribution at this point. Further probing of points in the DNS data (not shown) revealed that the fluctuations observed outside the aneurysmal sac were significantly more prevalent and higher in magnitude than those inside the aneurysmal sac. The probe point shown in Fig. (9a) maintained the largest high frequency fluctuations of any probe point evaluated. Though, it is important to note that due to the

computational complexity of the DNS data, not all points were evaluated so it is plausible that a point with larger high frequency fluctuations in the aneurysm flow field existed. Fig. (9b) shows all STB particle tracks which passed through the specific DNS probe point outside the aneurysmal sac. Meanwhile Fig. (9c) shows all STB particle tracks which passed through a probe point inside the aneurysmal sac. Fig. (9b) and (9c) illustrate that the particles generally maintained longer and smoother paths in the 60 bpm case as compared to 137 bpm. This can be attributed to the increase in overall fluctuations present in the system (not high frequency fluctuations as being investigated here) resulting in the chaotic particle motions and consequent tracking loss. Hence, this highlights that differentiating high frequency fluctuations from noise in the STB tracks is a particular challenge. Additionally, since volumetric PTV is inherently a Lagrangian approach to flow analysis, a new method for evaluating high frequency fluctuations within such framework needs to be identified. It is important to note that although the particle tracks can be converted to an Eulerian flow field through a gridding process, this computation involves inherent smoothing and averaging. Thus, the Lagrangian particle tracks provide the highest fidelity data to observe high frequency fluctuations. Given this, in this work, we investigated the possibility of evaluating the Eulerian flow fluctuations (as done with the DNS) from a Lagrangian perceptive using various signal processing tools.

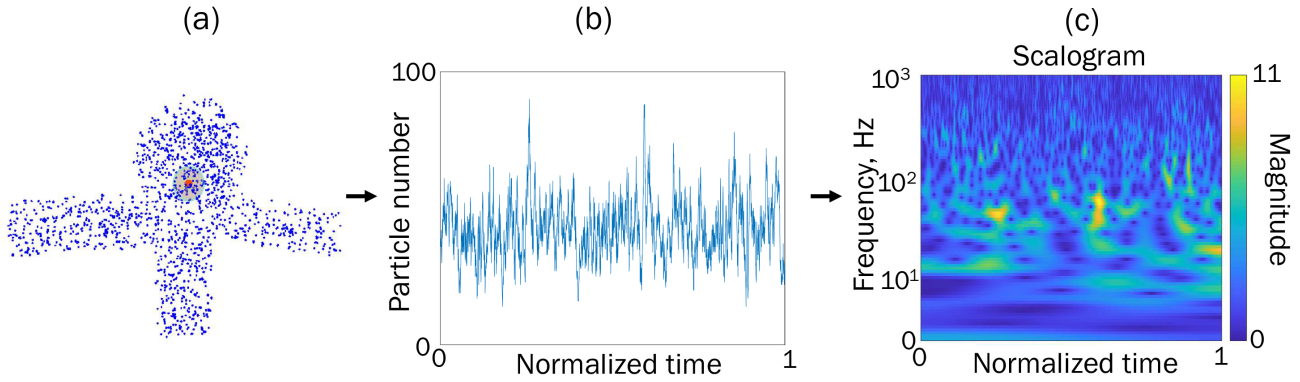

Figure 10. The proposed method for evaluating high frequency velocity fluctuations using STB data. (a) The creation of a sphere around the probe point in the volumetric PTV data. (b) Temporal variation of the number particles in the created sphere. (c) CWT scalogram of the number of particles in the sphere.

Fig. (10) illustrates the proposed method to evaluate the high frequency velocity fluctuations from a Lagrangian framework. First, a probe point is selected, and a sphere around this probe point is identified (Fig. (10)a). The radius of the sphere was chosen to ensure that sufficient particles will be present within the sphere while maintaining the localization information corresponding to the probe point. Herein, we set the sphere radius as 1 mm. Next, the number of particles present inside the sphere at each time instant and the temporal variation of the number of particles are calculated (Fig. (10)b). Since the velocity fluctuations at a probe induce fluctuations in the particle positions, the variation in the number of particles inside the sphere is expected to provide

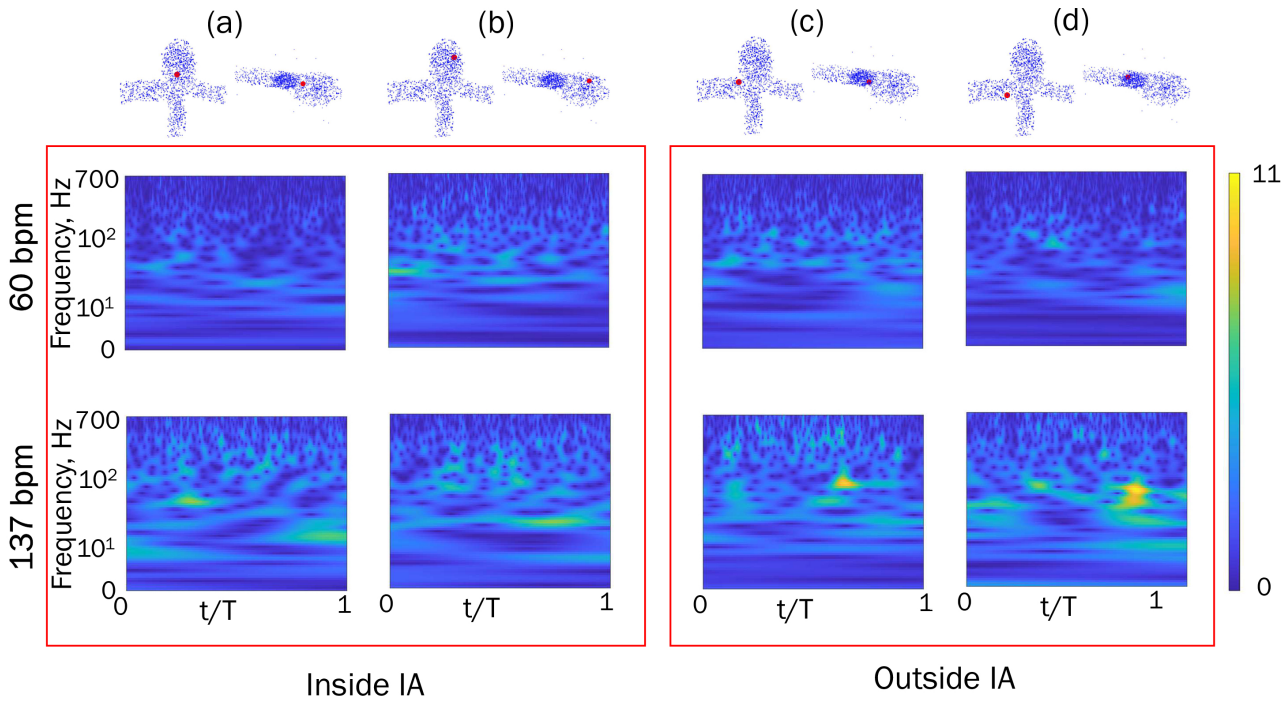

Figure 11. Time-frequency analysis of the variation in number of particles within sphere probe points both inside and outside the aneurysmal sac.

an indirect measurement to the flow fluctuations. Hence, a time-frequency analysis, as illustrated in Fig. (10c), can be used to evaluate the frequency of such variations. Specifically, the continuous wavelet transform (CWT) was employed to obtain the time-frequency representation (TFR). Finally, the presence of high frequency components over time were investigated.

To investigate the efficacy of the method, we first calculated the TFR of the number of particle variation for various probes inside and outside of the aneurysmal sac for both the 60 bpm and 137 bpm cases. Figs. (11a) and (11b) show the TFR at two probes inside the aneurysmal sac, while Figs. (11c) and (11d) represent two probes outside the aneurysmal sac. Fig. (11) demonstrates that the 137 bpm case, in general, exhibited comparably higher involvement of high frequencies. The TFR magnitude of frequencies in general were also amplified as the heart rate increased. Quantitatively, an increase of 50% and 78% in the respective average amplitude and mean frequencies were observed across all frequencies and time instant as heart rate increased from 60 bpm to 137 bpm. The increase in the amplitude can be attributed to the increase in flow rate while the increase in the mean frequency can be attributed to the involvement of higher frequencies. Furthermore, for the 137 bpm case, the probe points outside the aneurysmal sac exhibited higher frequency components as compared to those inside the aneurysmal sac, particularly during the deceleration phase. Specifically, frequency components were calculated to be around 78 Hz and 59 Hz with occurrence around normalized time of 0.64 and 0.78 in the case of Figs. (11c) and (11d), respec-

tively. This observation was akin to the presence of velocity fluctuations in the deceleration phase at 137 bpm in the DNS simulation (Fig. (9a)), suggesting a potential association. Thus, the particle number variation at specific probe point method seems capable of capturing certain aspects of the associated local hemodynamic fluctuations. However, the precise relation between high frequency components in the proposed method and temporal velocity fluctuations remain incompletely understood at this stage. Consequently, predicting velocity fluctuations in the presence of these high frequency components in the proposed method is inconclusive with the current dataset. The challenge in verification arises from the high resolution of DNS, the noise from experiments, and the inherent loss of particle tracks at higher bpm cases. Hence, a new mathematically sound methodology based on the Lagrangian-Euler framework conversion is necessary to accurately establish the association with velocity fluctuations. Furthermore, a high-resolution particle track capture of the relevant probe points is needed to validate any methodology experimentally. Further investigation into such a methodology and experimental setup will be explored in future work.

4. Conclusion

In this work, we investigated the effect of the heart rate and inflow amplitude on the velocity field, vorticity and TKE in and around a patient-specific R MCA IA using 4D PTV. Additionally, we investigated the presence of high frequency fluctuation in the flow using DNS and attempted to evaluate these fluctuations using the 4D PTV dataset. In general, we observed that an increase in heart rate led to a stronger and more concentrated inflow jet while a decrease in heart rate was associated with non-uniformity in the velocity field of the outlets, indicating a potential trade-off between aneurysmal sac and vascular remodeling. Furthermore, the higher heart rate case was associated with strong, larger, and asymmetrical vorticity structures compared to the lower heart rate case. Further investigation into the vortical structures suggested the presence of disturbed flow and high frequency fluctuations at the junction region between aneurysmal sac and outflow vessels. The investigation into TKE further reinforced the association of vortical structures with disturbed flow and strongly implied the presence of high frequency fluctuation components at higher heart rate. To evaluate the presence of fluctuation components, we proposed a Lagrangian-based approach in addition to using a DNS simulation. While the proposed method extracted certain aspects of the velocity fluctuation component, establishing a precise relation to high frequency components requires a more mathematically sound methodology and a higher resolution experimental setup.

Acknowledgements

The authors would like to acknowledge support from an American Heart Association (AHA) Career Development Award (94035).

References

Abdelsamie, A., Fru, G., Oster, T., Dietzsch, F., Janiga, G., & Thévenin, D. (2016). Towards direct numerical simulations of low-Mach number turbulent reacting and two-phase flows using immersed boundaries. *Computers & Fluids*, *131*, 123–141. (Publisher: Elsevier)

Baek, H., Jayaraman, M., Richardson, P., & Karniadakis, G. (2010). Flow instability and wall shear stress variation in intracranial aneurysms. *Journal of the Royal Society Interface*, *7*(47), 967–988. (Publisher: The Royal Society)

Berg, P., Stucht, D., Janiga, G., Beuing, O., Speck, O., & Thévenin, D. (2014). Cerebral blood flow in a healthy Circle of Willis and two intracranial aneurysms: computational fluid dynamics versus four-dimensional phase-contrast magnetic resonance imaging. *Journal of biomechanical engineering*, *136*(4), 041003. (Publisher: American Society of Mechanical Engineers)

Boussel, L., Rayz, V., McCulloch, C., Martin, A., Acevedo-Bolton, G., Lawton, M., ... Saloner, D. (2008, November). Aneurysm Growth Occurs at Region of Low Wall Shear Stress: Patient-Specific Correlation of Hemodynamics and Growth in a Longitudinal Study. *Stroke*, *39*(11), 2997–3002. Retrieved 2023-03-24, from https://www.ahajournals.org/doi/10.1161/STROKEAHA.108.521617 doi: 10.1161/STROKEAHA.108.521617

Bowker, T., Watton, P., Summers, P., Byrne, J., & Ventikos, Y. (2010). Rest versus exercise hemodynamics for middle cerebral artery aneurysms: a computational study. *American journal of neuroradiology*, *31*(2), 317–323. (Publisher: Am Soc Neuroradiology)

Brindise, M. C., Busse, M. M., & Vlachos, P. P. (2018, November). Density- and viscosity-matched Newtonian and non-Newtonian blood-analog solutions with PDMS refractive index. *Experiments in Fluids*, *59*(11), 173. Retrieved 2023-03-24, from http://link.springer.com/10.1007/s00348-018-2629-6 doi: 10.1007/s00348-018-2629-6

Brindise, M. C., Rothenberger, S., Dickerhoff, B., Schnell, S., Markl, M., Saloner, D., ... Vlachos, P. P. (2019). Multi-modality cerebral aneurysm haemodynamic analysis: in vivo 4D flow MRI, in vitro volumetric particle velocimetry and in silico computational fluid dynamics. *Journal of the Royal Society Interface*, *16*(158), 20190465. (Publisher: The Royal Society)

Brindise, M. C., & Vlachos, P. P. (2017). Proper orthogonal decomposition truncation method for data denoising and order reduction. *Experiments in Fluids*, *58*, 1–18. (Publisher: Springer)

Brindise, M. C., & Vlachos, P. P. (2018). Pulsatile pipe flow transition: Flow waveform effects. *Physics of Fluids*, *30*(1). (Publisher: AIP Publishing)

Brisman, J. L., Song, J. K., & Newell, D. W. (2006). Cerebral aneurysms. *New England journal of medicine*, *355*(9), 928–939. (Publisher: Mass Medical Soc)

Cebral, J. R., Duan, X., Gade, P. S., Chung, B. J., Mut, F., Aziz, K., & Robertson, A. M. (2016, December). Regional Mapping of Flow and Wall Characteristics of Intracranial Aneurysms. *Annals of Biomedical Engineering*, *44*(12), 3553–3567. Retrieved 2023-03-24, from http://link.springer.com/10.1007/s10439-016-1682-7 doi: 10.1007/s10439-016-1682-7

Cebral, J. R., Mut, F., Weir, J., & Putman, C. (2011b). Quantitative characterization of the hemodynamic environment in ruptured and unruptured brain aneurysms. *American Journal of Neuroradiology*, *32*(1), 145–151. (Publisher: Am Soc Neuroradiology)

Cebral, J. R., Mut, F., Weir, J., & Putman, C. M. (2011a). Association of hemodynamic characteristics and cerebral aneurysm rupture. *American Journal of Neuroradiology*, *32*(2), 264–270. (Publisher: Am Soc Neuroradiology)

Cebral, J. R., & Raschi, M. (2013). Suggested connections between risk factors of intracranial aneurysms: a review. *Annals of biomedical engineering*, *41*, 1366–1383. (Publisher: Springer)

Dabagh, M., Nair, P., Gounley, J., Frakes, D., Gonzalez, L. F., & Randles, A. (2019, July). Hemodynamic and morphological characteristics of a growing cerebral aneurysm. *Neurosurgical Focus*, *47*(1), E13. Retrieved 2024-05-31, from https://thejns.org/view/journals/neurosurg-focus/47/1/article-pE13.xml doi: 10.3171/2019.4.FOCUS19195

Ferguson, G. G. (1970). Turbulence in human intracranial saccular aneurysms. *Journal of neurosurgery*, *33*(5), 485–497. (Publisher: Journal of Neurosurgery Publishing Group)

Ford, M. D., & Piomelli, U. (2012, September). Exploring High Frequency Temporal Fluctuations in the Terminal Aneurysm of the Basilar Bifurcation. *Journal of Biomechanical Engineering*, *134*(9), 091003. Retrieved 2024-05-31, from https://asmedigitalcollection.asme.org/biomechanical/article/doi/10.1115/1.4007279/455032/Exploring-High-Frequency-Temporal-Fluctuations-in doi: 10.1115/1.4007279

Jiang, J., & Strother, C. (2009). Computational fluid dynamics simulations of intracranial aneurysms at varying heart rates: a "patient-specific" study.

Khan, M., Arana, V. T., Najafi, M., MacDonald, D., Natarajan, T., Valen-Sendstad, K., & Steinman, D. (2021). On the prevalence of flow instabilities from high-fidelity computational fluid dynamics of intracranial bifurcation aneurysms. *Journal of Biomechanics*, *127*, 110683. (Publisher: Elsevier)

Kojima, M., Irie, K., Ikeda, S., Fukuda, T., Arai, F., Hirose, Y., & Negoro, M. (2012). The hemodynamic study for growth factor evaluation of rupture cerebral aneurysm followed up for five years. *Journal of Biomedical Science and Engineering*, *05*(12), 884–891. Retrieved 2023-03-24, from http://www.scirp.org/journal/doi.aspx?DOI=10.4236/jbise.2012.512A112 doi: 10.4236/jbise.2012.512A112

Mayberg, M. R., Batjer, H. H., Dacey, R., Diringer, M., Haley, E. C., Heros, R. C., ... Feinberg, W. (1994, November). Guidelines for the management of aneurysmal subarachnoid hemorrhage. A statement for healthcare professionals from a special writing group of the Stroke Council, American Heart Association. *Circulation*, *90*(5), 2592–2605. Retrieved 2024-05-31, from https://www.ahajournals.org/doi/10.1161/01.CIR.90.5.2592 doi: 10.1161/01.CIR.90.5.2592

Meng, H., Tutino, V., Xiang, J., & Siddiqui, A. (2014). High WSS or low WSS? Complex interactions of hemodynamics with intracranial aneurysm initiation, growth, and rupture: toward a unifying hypothesis. *American Journal of Neuroradiology*, *35*(7), 1254–1262. (Publisher: Am Soc Neuroradiology)

Qian, Y., Takao, H., Umezu, M., & Murayama, Y. (2011, November). Risk Analysis of Unruptured Aneurysms Using Computational Fluid Dynamics Technology: Preliminary Results. *American Journal of Neuroradiology*, *32*(10), 1948–1955. Retrieved 2023-03-24, from http://www.ajnr.org/lookup/doi/10.3174/ajnr.A2655 doi: 10.3174/ajnr.A2655

Rinkel, G. J. E., Djibuti, M., Algra, A., & Van Gijn, J. (1998, January). Prevalence and Risk of Rupture of Intracranial Aneurysms: A Systematic Review. *Stroke*, *29*(1), 251–256. Retrieved 2024-05-31, from https://www.ahajournals.org/doi/10.1161/01.STR.29.1.251 doi: 10.1161/01.STR.29.1.251

Roach, M. R., Scott, S., & Ferguson, G. G. (1972). The hemodynamic importance of the geometry of bifurcations in the circle of Willis (glass model studies). *Stroke*, *3*(3), 255–267. (Publisher: Am Heart Assoc)

Roloff, C., Stucht, D., Beuing, O., & Berg, P. (2019). Comparison of intracranial aneurysm flow quantification techniques: standard PIV vs stereoscopic PIV vs tomographic PIV vs phase-contrast MRI vs CFD. *Journal of neurointerventional surgery*, *11*(3), 275–282. (Publisher: British Medical Journal Publishing Group)

Saqr, K. M., Tupin, S., Rashad, S., Endo, T., Niizuma, K., Tominaga, T., & Ohta, M. (2020, September). Physiologic blood flow is turbulent. *Scientific Reports*, *10*(1), 15492. Retrieved 2023-03-24, from https://www.nature.com/articles/s41598-020-72309-8 doi: 10.1038/s41598-020-72309-8

Sarrami-Foroushani, A., Esfahany, M. N., Rad, H. S., Firouznia, K., Shakiba, M., & Ghanaati, H. (2016). Effects of variations of flow and heart rate on intra-aneurysmal hemodynamics in a ruptured internal carotid artery aneurysm during exercise. *Iranian Journal of Radiology*, *13*(1). (Publisher: Brieflands)

Schanz, D., Gesemann, S., & Schröder, A. (2016). Shake-The-Box: Lagrangian particle tracking at high particle image densities. *Experiments in fluids*, *57*, 1–27. (Publisher: Springer)

Schievink, W. I. (1997, January). Intracranial Aneurysms. *New England Journal of Medicine*, *336*(1), 28–40. Retrieved 2024-05-31, from http://www.nejm.org/doi/abs/10.1056/NEJM199701023360106 doi: 10.1056/NEJM199701023360106

Sekhar, L. N., & Wasserman, J. F. (1984). Noninvasive detection of intracranial vascular lesions using an electronic stethoscope. *Journal of neurosurgery*, *60*(3), 553–559. (Publisher: Journal of Neurosurgery Publishing Group)

Sirovich, L. (1989, July). Chaotic dynamics of coherent structures. *Physica D: Nonlinear Phenomena*, *37*(1-3), 126–145. Retrieved 2024-05-31, from https://linkinghub.elsevier.com/retrieve/pii/0167278989901231 doi: 10.1016/0167-2789(89)90123-1

Steiger, H., & Reulen, H. J. (1986). Low frequency flow fluctuations in saccular aneurysms. *Acta neurochirurgica*, *83*, 131–137. (Publisher: Springer)

Steiger, H. J., Liepsch, D. W., Poll, A., & Reulen, H. J. (1988). Hemodynamic stress in terminal saccular aneurysms: a laser-Doppler study. *Heart and vessels*, *4*, 162–169. (Publisher: Springer)

Steiger, H. J., Poll, A., Liepsch, D., & Reulen, H.-J. (1987). Basic flow structure in saccular aneurysms: a flow visualization study. *Heart and vessels*, *3*, 55–65. (Publisher: Springer)

Trip, R., Kuik, D. J., Westerweel, J., & Poelma, C. (2012, January). An experimental study of transitional pulsatile pipe flow. *Physics of Fluids*, *24*(1), 014103. Retrieved 2023-03-24, from http://aip.scitation.org/doi/10.1063/1.3673611 doi: 10.1063/1.3673611

Valen-Sendstad, K., Mardal, K.-A., Mortensen, M., Reif, B. A. P., & Langtangen, H. P. (2011). Direct numerical simulation of transitional flow in a patient-specific intracranial aneurysm. *Journal of biomechanics*, *44*(16), 2826–2832. (Publisher: Elsevier)

Valen-Sendstad, K., Mardal, K.-A., & Steinman, D. A. (2013). High-resolution CFD detects high-frequency velocity fluctuations in bifurcation, but not sidewall, aneurysms. *Journal of biomechanics*, *46*(2), 402–407. (Publisher: Elsevier)

Valen-Sendstad, K., Piccinelli, M., & Steinman, D. A. (2014). High-resolution computational fluid dynamics detects flow instabilities in the carotid siphon: implications for aneurysm initiation and rupture? *Journal of biomechanics*, *47*(12), 3210–3216. (Publisher: Elsevier)

Varble, N., Xiang, J., Lin, N., Levy, E., & Meng, H. (2016, June). Flow Instability Detected by High-Resolution Computational Fluid Dynamics in Fifty-Six Middle Cerebral Artery Aneurysms. *Journal of Biomechanical Engineering*, *138*(6), 061009. Retrieved 2024-05-31, from https://asmedigitalcollection.asme.org/biomechanical/article/doi/10.1115/1.4033477/371287/Flow-Instability-Detected-by-HighResolution doi: 10.1115/1.4033477

Vlak, M. H., Algra, A., Brandenburg, R., & Rinkel, G. J. (2011, July). Prevalence of unruptured intracranial aneurysms, with emphasis on sex, age, comorbidity, country, and time period: a systematic review and meta-analysis. *The Lancet Neurology*, *10*(7), 626–636. Retrieved 2024-05-31, from https://linkinghub.elsevier.com/retrieve/pii/S1474442211701090 doi: 10.1016/S1474-4422(11)70109-0

Westerweel, J., & Scarano, F. (2005). Universal outlier detection for PIV data. *Experiments in fluids*, *39*, 1096–1100. (Publisher: Springer)

Wieneke, B. (2008). Volume self-calibration for 3D particle image velocimetry. *Experiments in fluids*, *45*(4), 549–556. (Publisher: Springer)

Xiang, J., Natarajan, S. K., Tremmel, M., Ma, D., Mocco, J., Hopkins, L. N., ... Meng, H. (2011). Hemodynamic–morphologic discriminants for intracranial aneurysm rupture. *Stroke*, *42*(1), 144–152. (Publisher: Am Heart Assoc)

Xu, D., & Avila, M. (2018, December). The effect of pulsation frequency on transition in pulsatile pipe flow. *Journal of Fluid Mechanics*, *857*, 937–951. Retrieved 2023-06-20, from https://www.cambridge.org/core/product/identifier/S0022112018007899/type/journal_article doi: 10.1017/jfm.2018.789

Yagi, T., Sato, A., Shinke, M., Takahashi, S., Tobe, Y., Takao, H., ... Umezu, M. (2013). Experimental insights into flow impingement in cerebral aneurysm by stereoscopic particle image velocimetry: transition from a laminar regime. *Journal of the Royal Society Interface*, *10*(82), 20121031. (Publisher: The Royal Society)